Coupled Aerostructural Topology Optimization Using a Level Set Method for 3D Aircraft Wings[1]

Peter D. Dunning*
National Institute of Aerospace, Hampton, VA, 23666
* Corresponding author Email: p.d.dunning@bath.ac.uk Tel: +441225384389
Bret K. Stanford
NASA Langley Research Center, Hampton, VA, 23681

H. Alicia Kim
University of Bath, Bath, United Kingdom, BA2 7AY

Abstract
The purpose of this work is to develop a level set topology optimization method for an unstructured three-dimensional mesh and apply it to wing box design for coupled aerostructural considerations. The paper develops fast marching and upwind schemes suitable for unstructured meshes, which make the level set method robust and efficient. The method is applied to optimize a representative wing box internal structure for the NASA Common Research Model. The objective is to minimize the total compliance of the wing box. The trim condition that aerodynamic lift must balance the total weight of the aircraft is enforced by allowing the root angle of attack to change. The adjoint method is used to obtain the coupled shape sensitivities required to perform aerostructural optimization of the wing box. Optimum solutions for several aerodynamic and body force load cases, as well as a ground load case, are presented.

Nomenclature
A = sensitivity factor for angle of attack
$\boldsymbol{a}$ = vector of Doublet Lattice Method (DLM) box areas
$\boldsymbol{b}$ = vector defining influence of wing deformed shape on lift
C = compliance of the structure
$\boldsymbol{c_p}$ = pressure coefficient vector
$\boldsymbol{D}$ = aerodynamic influence coefficient matrix
E = material property tensor
e = number of elements attached to a node
$\boldsymbol{f_a}$ = aerodynamic load vector
$\boldsymbol{f_g}$ = body force load vector
$\boldsymbol{f_t}$ = total load vector
g = acceleration due to gravity
h = element edge length
i, j = indices
$\boldsymbol{K}$ = global structural stiffness matrix
$\boldsymbol{K_c}$ = stiffness matrix of an element cut by the boundary
$\boldsymbol{K_E}$ = stiffness matrix of a finite element
k = iteration number
L = total lift force

[1] An earlier version of this work was presented at the AIAA SciTech Conference 2014.

L_c = lift force from built-in twist and camber
L_α = lift force from unit angle of attack
N = load factor
n = unit normal vector
p = adjoint state vector
q = dynamic pressure
$\boldsymbol{Q}$ = aerodynamic stiffness matrix
$\boldsymbol{S}$ = force transfer matrix
$\boldsymbol{T}$ = displacement transfer matrix
t = fictitious time variable
u = displacement field or vector
V_n = velocity function
v = virtual displacement
W_b = wing box weight
W_c = fixed aircraft weight
$\boldsymbol{w}$ = downwash dependent on deformed wing shape
$\boldsymbol{w_c}$ = constant downwash from built-in camber
x = point in the design domain
$\boldsymbol{z}$ = column vector of 1's
α = angle of attack
β_c = volume of a cut element that lies inside the structure
β_E = volume of an element
γ = small number
Γ = structural boundary
Γ_D = part of boundary subject to displacement boundary conditions
Γ_N = part of boundary subject to aerodynamic loads
Γ_0 = part of boundary free from boundary conditions and aerodynamic loads
Δt = time step
ε = strain tensor
θ = arbitrary vector (shape derivative auxiliary variable)
ρ = material density
ϕ = implicit function
Ω_d = design domain
Ω = structural domain

Keywords: Level set method, 3D unstructured mesh, topology optimization, multi-disciplinary optimization.

1. Introduction

This paper has two main objectives. The first is to develop a method for preforming level set topology optimization on an unstructured three dimensional (3D) grid. This method is then employed to minimize the compliance of a wing box under coupled aerostructural and body force loads.

1.1 Topology optimization in aircraft design

Topology optimization is the most general form of structural optimization, as it is the least restricted by pre-determined design variables (Bendsøe and Sigmund 2003). Topology optimization has been used as a tool for improving aircraft wing designs. However, the full potential of topology optimization is often not realized, as the design space is limited to a pre-determined layout or applied only to local regions or sub-components. For example, Balabanov and Haftka (1996) used truss topology optimization to design the internal structure of a wing, where the discrete ground structure limits the design space. The Solid Isotropic Material with Penalization (SIMP) method has been used to optimize a rib and spar type wing structure, where the layout of ribs and spars was fixed (Maute and Allen 2004; Stanford and Dunning 2014). The bubble method has been used to optimize the layout of a single rib for a set of loadings obtained from pull-up maneuvers and tank pressures (Eschenauer and Olhoff 2001). The SIMP method has also been used to optimize individual ribs (Krog et al. 2004). The spectral level set method has been applied to optimize the reinforcement of a wing upper skin to maximize aileron reversal dynamic pressure (Gomes and Suleman 2008). Topology optimization has also been applied to the design of plate-like wings, through varying the thickness of the plate (Stanford and Beran 2011; De Leon et al. 2012) or varying the distribution of different materials (Stanford and Ifju 2009).

There are few examples of topology optimization being employed to design the entire wing box structure. The approach by Eves et al. (2009) utilizes topology optimization to design the layout of major internal structural members. This involves using topology optimization to design spar type members for maximum stiffness under static aerodynamic loading with deflection, manufacturing and volume constraints. A separate stage of rib pitch optimization is then used to prevent skin buckling. There are also examples of SIMP being used to explore optimal internal wing structures (Krog et al. 2009; Oktay et al. 2014). The aim of this paper is to consider the entire 3D wing box space as the design domain for topology optimization to explore novel configurations for the entire wing box structure.

Another important consideration in topology optimization of aircraft wings is the aerostructural coupling between the aerodynamics and the deformed shape of the wing. Some approaches compute the pressure loading for an assumed wing shape and do not account for the coupling (Balabanov and Haftka 1996; Eschenauer and Olhoff 2001; Eves et al. 2009; Oktay et al. 2011). However, this coupling effect can strongly influence the optimal design (Maute and Allen 2004). James et al. (2014) used a multidisciplinary framework that optimized both the aerodynamic shape of the wing and the topology of the wing box structure using the SIMP method. However, the optimal designs contained a significant amount of intermediate density material, which can be difficult to interpret as a manufacturable design, which was also noticed by Maute and Allen (2004). An alternative is to use a level set topology optimization method (Allaire et al. 2004; Wang et al. 2003; Dunning and Kim 2013), where the boundary of the structure is defined using an implicit function, which produces solutions with clear boundaries.

1.2 Level set topology optimization

There are various approaches to level set based topology optimization that have emerged in the last decade. The interested reader is referred to the reviews by Deaton and Grandhi (2014) and van Dijk et al. (2013) and the critical comparison of several methods by Gain and Paulino

(2013). The level set method employed in this work uses shape sensitivity analysis coupled with the level set method originally developed for implicit front tracking (Sethian 1999; Osher and Fedkiw 2003). In this approach the implicit function is a signed distance function and it is updated by solving a Hamilton-Jacobi (H-J) type equation using an explicit upwind scheme (Allaire et al. 2004; Wang et al. 2003). This is sometimes called the conventional or direct approach (Deaton and Grandhi 2014). Although the conventional level set method is based on shape optimization, the implicit boundary representation allows natural handling of topological changes, such as merging, splitting and closing of holes. However, it is not native to the level set method to specifically insert a new hole. Therefore, special techniques are usually required to create new holes during optimization (Dunning and Kim 2013; Allaire et al 2005). Interestingly, new holes can naturally emerge in three dimensional problems by the crossing of two separate level set surfaces (Allaire et al. 2004).

The application of the level set method for wing structure optimization has been limited to local regions (Gomes and Suleman 2008) or did not account for the aerostructural coupling (James and Martins 2012). In our previous work, the level set method was used to optimize the internal structure of a 3D wing box and included the effect of aerostructural interaction through coupled analysis and coupled sensitivities (Dunning et al. 2013). However, the effect of body force loading was not included, the level set method was implemented on a uniform Cartesian grid and the examples were limited to cuboid design domains. Also, the angle of attack was fixed and the trim condition that lift must equal to weight was imposed as a constraint.

To optimize the internal structure of more realistic wings, such as the Common Research Model (CRM) (Vassberg et al. 2008), a level set method for more general design domains that are non-rectangular needs to be developed. One approach is to immerse the general design domain in a larger uniform level set grid and maintain the shape of the actual design domain by fixing the implicit function in the region of its boundary (Brampton et al. 2012). Another approach is to map the general design domain to a uniform grid, for example by using an isoparametric transform (James and Martins 2012). However, this is only applicable when a mapping is available and the mesh is structured. A third approach is to implement a level set framework that can naturally handle unstructured meshes within arbitrary domain shapes. Examples of the third approach are rare for conventional level set based optimization methods. The streamline diffusion Finite Element Method (FEM) was used to solve the H-J equation, instead of the usual finite difference upwind schemes, and also to compute the re-initialization of the implicit function (Xing et al. 2010). This method is suitable for unstructured meshes as it is FE based. Another method suitable for unstructured meshes is to use a geometry based re-initialization procedure with a FE based solution for the implicit function update (Yamasaki et al. 2010). However, both these approaches can be computationally expensive when considering large 3D applications.

1.3 Overview of the paper

The two main novel contributions of this paper are the development of a method for conventional level set topology optimization on a 3D unstructured grid for an aircraft wing and the topology optimization subject to coupled aerostructural loading and self-weight body force. The design space for the 3D level set optimization is the volume contained within the wing box and the optimization can choose any structure within that space. Thus, the approach is not

limited by any pre-determined structural layout, such as ribs and spars. The 3D unstructured grid level set method developed in this work combines the efficient fast marching method and an upwind finite difference scheme to solve the H-J equation. The unstructured fast marching method introduced in this paper is an extension of the method developed by Sethian & Vladimirsky (2000). Although applied to wing box design, the level set topology optimization approach developed in this paper has the potential to be applied to solve general problems.

This paper is organized as follows. Section 2 briefly reviews salient details of the conventional level set method, followed by the development of numerical techniques for unstructured 3D grids and an illustrative example. Section 3 introduces the minimization of compliance problem with coupled aerodynamic and body force loading, followed by details of the aeroelastic model, shape sensitivity analysis and solution procedure for the primary and adjoint equations. Section 4 employs the unstructured 3D level set method, developed in Section 2, to solve various minimization of compliance problems for a 3D wing box, based on the CRM. Conclusions are provided in Section 5.

2. Level Set Topology Optimization

A 3D level set method was used to optimize the internal structure of the wing box. A conventional level set method was employed. The basic method is briefly outlined followed by details of our development for an unstructured mesh implementation. First, the boundary of the structure is defined as the zero level set of an implicit function:

$$\begin{cases} \phi(x) \geq 0, x \in \Omega \\ \phi(x) = 0, x \in \Gamma \\ \phi(x) < 0, x \notin \Omega \end{cases} \tag{1}$$

where $\phi(x)$ is the implicit function and $x \in \Omega_d$, where Ω_d is the design domain containing the structure, $\Omega \subset \Omega_d$. The implicit description of the structure allows the boundary to break and merge naturally, allowing topological changes to occur during optimization.

The level set description of the structural boundary can be used for optimization. First, a velocity field is derived from shape sensitivity analysis. The implicit function is then updated by solving a H-J type equation:

$$\frac{\partial \phi(x)}{\partial t} + \nabla \phi(x,t) \frac{dx}{dt} = 0 \tag{2}$$

where t is a fictitious time domain. Equation (2) can be discretized and rearranged to provide a convenient update formula for optimization:

$$\phi_i^{k+1} = \phi_i^k - \Delta t \left| \nabla \phi_i^k \right| V_{n,i} \tag{3}$$

where i is a discrete point within the domain, k is the current iteration number, V_n is a velocity function defined normal to the boundary, such that a positive velocity moves the boundary inwards, and Δt is a discrete time step. Note that Eq. (3) is the same as solving Eq. (2) using an explicit forward Euler scheme (Osher and Fedkiw 2003).

2.1 Fixed Mesh Finite Element Analysis

The design domain is discretized using isoparametric hexahedral elements with the implicit function defined at the nodes. The same mesh is also utilized for the finite element analysis (FEA) of the wing box. Elements with incompatible modes are used to analyze the wing box structure, as these elements perform better in bending compared with standard tri-linear isoparametric elements (Cook et al. 2002).

The implicit function is interpolated within elements using standard tri-linear shape functions, which is useful for finding the exact position of the boundary. The implicit function is initialized as a signed distance function, where the value of the implicit function indicates the distance to the boundary and the sign is defined by Eq. (1). Details of how the signed distance function is computed for an unstructured mesh are included in Section 2.2. Maintaining a signed distance function throughout the optimization is important for the stability of the level set method (Sethian 1999; Osher and Fedkiw 2003). Otherwise the implicit function can become too steep or shallow, leading to numerical difficulties when solving the discretized H-J equation, Eq. (3).

For efficiency, the finite element mesh remains fixed during optimization. Therefore, some elements can be cut by the structure boundary leading to a discontinuity in material properties within the element. Discontinuous elements are treated using a volume-fraction weighted approximation for the element stiffness matrix:

$$\boldsymbol{K}_c = \left(\beta_c / \beta_E\right) \boldsymbol{K}_E \tag{4}$$

where K_c is the approximated stiffness matrix of the cut element, K_E is the stiffness matrix of the same element without a cut, whose volume is β_E, and β_c is the volume of the cut element that lies inside the structure. To compute the internal volume of a cut element, β_c, the hexahedral element is first divided into 24 sub-tetrahedra, Fig. 1. The implicit function is then interpolated onto the vertices of each sub-tetrahedron. The internal volume for each sub-tetrahedron can then be analytically computed and summed to obtain total value for the element. This is similar to the method proposed by Min and Gibou (2007), although their method used five sub-tetrahedra. The choice of 24 sub-tetrahedra eliminates directional bias from the interpolation and leads to a more robust method, though the computational cost is higher than the five sub-tetrahedra approach.

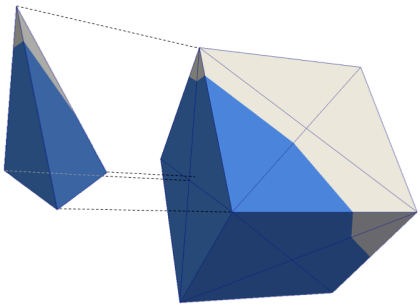

Figure 1. Numerical integration of inside volume by division into 24 sub-tetrahedra.

The total volume of the element, β_E, can be efficiently computed using an analytical formula (Grandy 1997). Elements that lie completely outside the boundary are assigned a small volume fraction, 10^{-6}. This is to avoid numerical difficulties involved when part of the structure becomes completely detached from the main structure, such that it can display rigid body motions. During our numerical studies the value of 10^{-6} was found to be sufficiently small, such that elements that were outside the structure did not provide significant stiffness or mass.

It is known that using the volume fraction method of Eq. (4) (also called the ersatz material approach) leads to reduced accuracy at the boundary due to the approximation of the element stiffness (Jang et al. 2004; Wei et al. 2010; Dunning et al. 2011). This is a concern for conventional level set methods, as the optimization is driven by shape sensitivities defined at the boundary. To overcome this problem, sensitivity values are computed at element Gauss points and interpolated at boundary points using a weighted least squares method using all Gauss point sensitivities within a specified radius of a boundary point (Dunning et al. 2011). This is modified for a non-Cartesian mesh by using Gauss point sensitivities inside elements that neighbor the element where the boundary point is located. A 2D example is shown in Fig. 2.

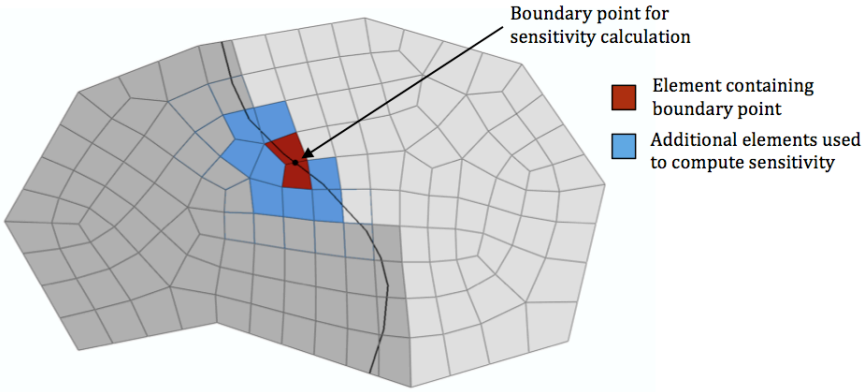

Figure 2. Boundary point sensitivity calculation for 2D unstructured mesh.

Boundary shape sensitivity values are computed at points where the boundary intersects an element edge and at nodes where the implicit function is zero. Boundary point shape sensitivities are then used to compute the velocity function. The derivation of the velocity function from shape sensitivities for the problem studied in this work is detailed in Section 3.3.

2.2 Velocity Extension and Re-initialization

A key aspect of conventional level set based optimization is the definition of the velocity function from the shape derivative. A shape derivative is characterized as a boundary integral of a shape sensitivity function multiplied by a velocity function (Allaire et al. 2004). Therefore, a shape derivative can only specify the velocity function at the boundary. However, to update the level set function using Eq. (3), discrete velocity values, $V_{n,i}$ are required at all discrete points i. A common approach in other conventional level set methods is to compute node velocities using a natural velocity extension method. This approach employs a fictitious material model, such as the ersatz material method (Allaire et al. 2004) or smoothed Heaviside function (Wang et al 2003), to compute shape sensitivity and velocity values at points that do not lie on the boundary. However, the natural velocity extension approach can lead to rapid degradation of the signed distance property and requires frequent re-initialization of the implicit function to maintain stability (Allaire et al. 2004; Gain and Paulino 2013). An alternative approach is taken here, where sensitivity and velocity values are only computed at the boundary. A velocity extension scheme is then used to compute node velocity values such that the signed distance property of the implicit function is maintained during the update. It has been observed that this approach requires significantly fewer signed distance re-initializations compared with the natural velocity extension method (Sethian 1999). A velocity extension strategy that maintains the signed distance function is to keep velocity values constant along a line normal to the boundary, which can be obtained by numerically solving (Osher and Fedkiw 2003):

$$\left(\partial V_n / \partial t\right) + sign\left(\phi\right)\left(\nabla\phi / \left|\nabla\phi\right|\right) \cdot \nabla V_n = 0 \tag{5}$$

One method to solve Eq. (5) is to choose an initial solution V_n and then employ an iterative procedure until convergence. This is performed in a pseudo-time domain that is different from the time axis used in the main level set evolution, Eq. (2). However, this approach can be computationally expensive. On Cartesian or rectilinear grids the velocity extension can be more efficiently computed using the fast marching method (Sethian 1999). The fast marching method has also been generalized by Sethian and Vladimirsky (2000) to solve Eikonal equations on unstructured meshes. Eikonal equations take the form:

$$\left\|\nabla\phi\right\| = F\left(x\right) \qquad in \qquad \Omega \tag{6}$$

where $F(x)$ is an arbitrary function. If $F(x) = 1$, then the solution of the Eikonal equation can be used to re-initialize the implicit function as a signed distance function, where the magnitude of the implicit function is found from solving Eq. (6) and the sign is defined by Eq. (1). However, the unstructured mesh fast marching method for solving Eikonal equations requires modification to obtain extension velocities. The method used by Sethian and Vladimirsky (2000) to solve the Eikonal equation for re-initialization is first summarized followed by details of how it is modified in this work to compute the extension velocities.

The fast marching method solves the Eikonal equation using an upwind finite difference scheme. The term upwind means that implicit function values are computed from information at points closer to the boundary. Thus, the solution is constructed in a progressive manner by marching out from the boundary. Finite differences are used to compute the spatial gradients of the implicit

function. During re-initialization $F(x) = 1$ in Eq. (6) and the implicit function value at a point is computed by solving:

$$\nabla\phi_i \cdot \nabla\phi_i = 1 \tag{7}$$

where the information used to construct the gradients is obtained from local points closer to the boundary. Thus, these points should already have implicit function values computed earlier, as they are closer to, or on the boundary. In 3D, up to three local points are used, as there are three spatial dimensions. If a node is near the boundary then the local points are locations where the boundary crosses an element edge attached to the node. Interpolation between two neighboring nodes with opposite implicit function sign is used to compute the location of a boundary point. If a node is not near the boundary, then the local points will be the nodes connected to the current node that are closer to the boundary. Due to the upwind scheme, the local points will have known implicit function values, computed during a previous step of the fast marching method.

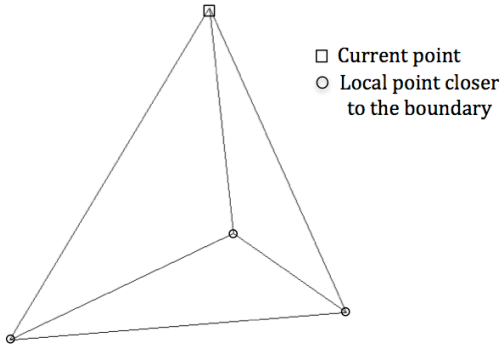

Figure 3. Local calculation of extension velocity in 3D.

To solve Eq. (7), a simplex is formed using the current node and the local points closer to the boundary, Fig. 3. The spatial gradients within the simplex are assumed constant and computed using linear shape functions, which is the same as using first order finite differences. For example, if the simplex is a tetrahedron, Fig. 3, the gradients of the implicit function are computed by obtaining the isoparametric gradient matrix, $[B]$, using the four-node tetrahedron shape functions (Cook et al. 2002):

$$\nabla\phi_i = \left[B\right]\left\{\phi\right\} \tag{8}$$

where $\{\phi\}$ is a vector of nodal values associated with the tetrahedron, Fig. 3. Using Eq. (8), Eq. (7) becomes:

$$\nabla\phi_i \cdot \nabla\phi_i = \left\{\phi\right\}^T \left[B\right]^T \left[B\right]\left\{\phi\right\} = 1 \tag{9}$$

The only unknown in Eq. (9) is the implicit function value at the current node, which can be obtained by solving a quadratic equation. It is often possible to form more than one simplex using neighboring nodes that are closer to the boundary. In this case, Eq. (9) is solved for each simplex and the one that produces the smallest magnitude implicit function value at the current node is the defining simplex for that node. The smallest value is chosen, as the magnitude of the

implicit function should be the shortest distance to the boundary. The defining simplex is then used in the fast marching scheme to compute the velocity extension. Equipped with a procedure for computing local solutions to Eq. (7), the fast marching method can be summarized as (Sethian and Vladimirsky 2000):

1. Compute local solutions for nodes with local points on the boundary, tag these as "known."
2. Find all "unknown" nodes connected to the "known" set, tag these as "considered."
3. Compute local solutions for the "considered" set of nodes.
4. Find the node in "considered" with the smallest magnitude of ϕ, tag this as "trial"
5. Find all nodes connected to "trial" that are not in "known" and update their local solutions, add these to the "considered" set and move the "trial" node to the "known" set.
6. If the "considered" set is empty, stop. Otherwise return to step 4.

The algorithm employed to compute extension velocities is developed from the fast marching method used to solve the Eikonal equation for re-initialization. The algorithm is similar and employs the same upwind and finite differencing techniques. The main difference is that after locally solving Eq. (7) for the implicit function value, the following is solved for the velocity function value at the current node using the defining simplex:

$$\nabla\phi_i \cdot \nabla V_{n,i} = 0 \tag{10}$$

where the spatial gradient of the velocity function is computed using linear shape functions as before:

$$\nabla V_{n,i} = \left[B\right]\left\{V_n\right\} \tag{11}$$

where $\{V_n\}$ is a vector of nodal velocity values associated with the locally constructed simplex. From Eqs. (8 ,10 & 11) we obtain:

$$\nabla\phi_i \cdot \nabla V_{n,i} = \left\{\phi\right\}^T \left[B\right]^T \left[B\right]\left\{V_n\right\} = 0 \tag{12}$$

Due to the upwind scheme, the only unknown in Eq. (12) is the velocity value at the current node. Thus, Eq. (12) can be rearranged and solved for the velocity value at the current node. Note that the implicit function values used in Eqs. (10-12) are those computed from first locally solving the Eikonal equation, Eq. (7), and not the current values, which remain unchanged during the computation of the velocity extension (Sethian 1999).

Sethian and Vladimirsky (2000) noted that the causality in the upwind scheme can be invalidated due to the presence of obtuse angles and this can cause numerical instability. This occurs because obtuse angles can result in information from nodes further from the boundary being used in the local solutions, Eqs. (9) & (12). We implement a check for upwind validity for each local solution to Eq. (7). First, the spatial gradient vector of the implicit function at the current point is computed using the new implicit function value and information from the other nodes in the

simplex. A solution is "upwind valid" if the negative of the spatial gradient vector points into the simplex (Sethian and Vladimirsky 2000). This indicates that the update of the implicit function at the current node came from within the simplex. If a simplex is not upwind valid, then it is not considered during the fast marching method. If there are no upwind valid simplexes immediately attached to a node, then a backtracking procedure is invoked. This involves searching backwards through the mesh towards the structure boundary and forming new simplexes using nodes with "known" implicit function values until an upwind valid simplex is found.

The backtracking procedure introduced in this work exploits the FE node-element connectivity. The local nodes attached to the current node will also be attached to other nodes defined by the FE mesh node-element connectivity. The other nodes with "known" implicit function values are then used to form new simplexes. The backtracking procedure starts by only considering simplexes that can be formed inside elements attached to the current node, illustrated in Fig. 4. This first step of the backtracking procedure is often sufficient to find an "upwind valid" simplex. If an "upwind valid" simplex is still not found, then further simplexes can be constructed using "known" nodes connected to the set of nodes already considered. The backtracking procedure can continue until an "upwind valid" simplex is found. In the event that backtracking completely fails, by exhausting all possible simplexes that can be formed from "known" nodes, then the default is to compute the implicit function value and velocity values using only information from the local node closest to the boundary. Backtracking beyond the first step can become computationally expensive, due to the increased number of simplexes that can be formed. However, in our experience, the first step is usually sufficient to form an "upwind valid" simplex. Therefore, a practical approach is taken where only the first step of the backtracking procedure is performed. If an "upwind valid" simplex is not found during the first step, the default is used instead of further backtracking.

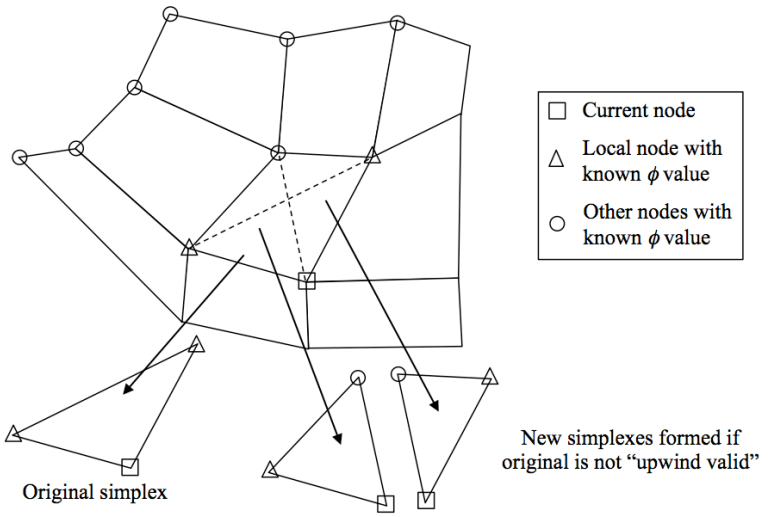

Figure 4. A 2D example of the backtracking procedure first step.

The velocity extension method aims to preserve the signed distance function. However, the implicit function may still loose the signed distance property during optimization, due to the approximations in the numerical implementation, such as the use of first order finite differences.

Therefore, the implicit function is re-initialized as a signed distance function at intervals of 30 iterations during the optimization.

2.3 Gradient of the Implicit Function

The spatial gradient of the implicit function at each node is also required to update the structure using Eq. (3). Again, we want to use an upwind scheme to compute the gradients and promote stability in the solution (Sethian 1999; Osher and Fedkiw 2003). Note that the required upwind gradients for solving the H-J equation are different from those computed during the fast marching method. In the fast marching method information was travelling outwards from the boundary, whereas the flow of information in the H-J equation depends on the sign of the velocity function. On a rectilinear grid, upwind schemes require a simple choice between forward or backward finite differences and the spatial gradient is computed using:

$$\left|\nabla\phi_i\right| = \max\left(sign(V_{n,i}),0\right)\nabla_i^+ - \min\left(sign(V_{n,i}),0\right)\nabla_i^- \tag{13a}$$

$$\nabla_i^+ = \left[\max\left(\nabla_i^{-x},0\right)^2 + \min\left(\nabla_i^{+x},0\right)^2 + \max\left(\nabla_i^{-y},0\right)^2 + \min\left(\nabla_i^{+y},0\right)^2 + \max\left(\nabla_i^{-z},0\right)^2 + \min\left(\nabla_i^{+z},0\right)^2\right]^{0.5} \tag{13b}$$

$$\nabla_i^- = \left[\min\left(\nabla_i^{-x},0\right)^2 + \max\left(\nabla_i^{+x},0\right)^2 + \min\left(\nabla_i^{-y},0\right)^2 + \max\left(\nabla_i^{+y},0\right)^2 + \min\left(\nabla_i^{-z},0\right)^2 + \max\left(\nabla_i^{+z},0\right)^2\right]^{0.5} \tag{13c}$$

where ∇_i^{-x} is the spatial gradient of the implicit function at node i in the $-x$ direction in Cartesian space. For a rectilinear grid the orthogonal gradient components used in Eq. (13) are simply computed using finite difference schemes. This is more difficult for a general unstructured meshes. In our implementation the gradient components are computed in the following manner. First a line is drawn from the node along the axis direction, for example along the negative x-axis. The finite element intersected by the line is then used to compute the gradient component for that axis direction using the tri-linear element shape functions. If there is no intersected element in an axis direction (i.e. the element lies on the domain boundary) then the intersected element in the opposite direction is used. If there no element in the opposite direction either, then any element connected to the current node is chosen to compute the gradient component. This approximation will only apply to nodes on the domain boundary.

2.4 The Level Set Topology Optimization Algorithm

The time step in Eq. (3) is computed using the well-known CFL condition for stability:

$$\Delta t = \min_i\left(0.9h_{\min,i} / V_{n,i}\right) \tag{14}$$

where $h_{min,i}$ is the shortest element edge length connected to node i.

A simple termination criterion is used, where the optimization is terminated if the maximum relative change in the objective over the previous ten iterations is less than a small number:

$$\left(C_{\max}^i - C_{\min}^i\right) / \left(C_{\max}^i + C_{\min}^i\right) < \gamma, \qquad i \in \left[k-9, k\right] \tag{15}$$

where C is the total compliance value, or objective, k is the iteration number and γ is a small number.

Finally, we summarize the optimization algorithm as the following major steps:

1. Assemble the global stiffness matrix from volume-fraction weighted element matrices, Eq. (4)
2. Solve the primary and adjoint equations (for the couple aerostructural case, see Section 3.4)
3. Check for convergence using Eq. (15). Otherwise continue.
4. Compute shape sensitivities at the boundary using a weighted least squares method (Section 2.1)
5. Obtain boundary velocity values from shape sensitivities (Eq. (39) for the aerostructural case)
6. Velocity extension using the fast marching method (Section 2.2)
7. Spatial gradient calculation using an upwind scheme (Section 2.3)
8. Update the implicit function by solving a H-J type equation, Eq. (3)

2.5 Example

The unstructured 3D mesh level set method developed above is demonstrated with a simple example. The compliance of a 3D cantilever beam is minimized subject to a material volume constraint. The design domain, loading and boundary conditions for the beam are shown in Fig. 5a. The material properties are Young's modulus of 200 and Poisson's ratio of 0.3. The upper limit on material volume is set to 40% of the total design domain. The example is solved using two meshes; the first is a structured mesh with 36 × 36 × 55 (71,280) elements, Fig. 5b, the second is an unstructured mesh with 69,190 elements, Fig. 5c. The solutions obtained for the structured and unstructured meshes are shown in Figs. 6a and 6b, respectively. Although the solutions are not identical, they are very similar and the final compliance values are within 1%, 0.4144 and 0.4110 for the structured and unstructured mesh solutions, respectively.

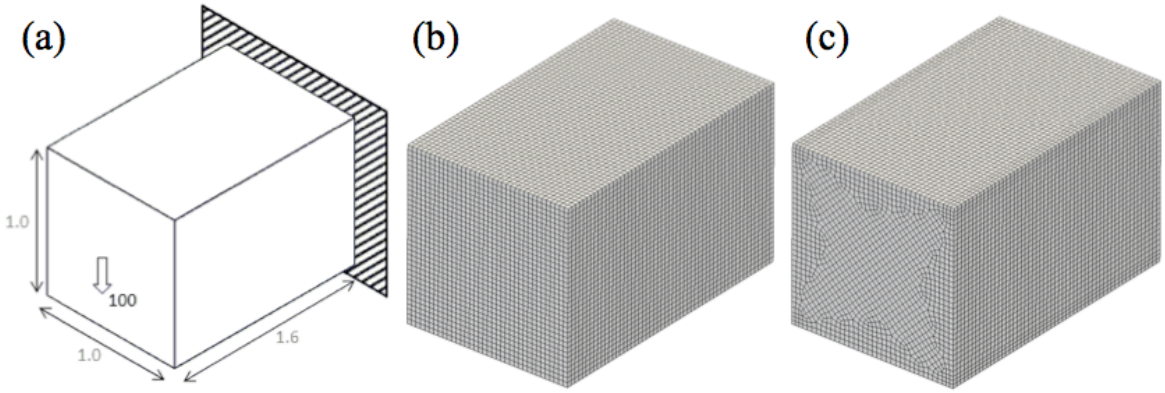

Figure 5. Beam example: a) Design domain, loading and boundary conditions, b) Structured mesh, c) Unstructured mesh.

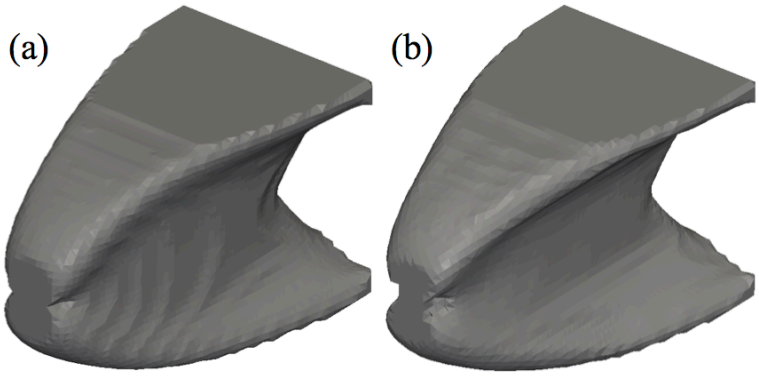

Figure 6. Beam example solutions: a) Structured mesh, b) Unstructured mesh.

3. Aerostructural Optimization Problem

The objective function studied in this work is to minimize the compliance of the internal wing box structure. The loading on the structure is composed of the lift force generated by a single flight condition and the weight of the wing. The lift distribution is dependent on the deformed shape of the wing, which is in turn dependent on the applied loading. Therefore, the aerodynamic loading is coupled to the structural response and the wing is part of a multi-disciplinary system. The wing is trimmed by allowing the root angle of attack to change so that the total lift force is equal to the total weight of the aircraft. The problem can be stated as:

$$\begin{aligned} &\underset{\Omega}{\text{Minimize}}: C(\boldsymbol{u},\Omega) = \boldsymbol{f}_t(\boldsymbol{u},\Omega)\cdot\boldsymbol{u} \\ &\text{Subject to: } \boldsymbol{K}(\Omega)\cdot\boldsymbol{u} = \boldsymbol{f}_t(\boldsymbol{u},\Omega) = \boldsymbol{f}_a(\boldsymbol{u},\Omega) + N\cdot\boldsymbol{f}_g(\Omega) \\ &\qquad\qquad L(\boldsymbol{u}) = N\cdot\left(W_b(\Omega) + W_c\right) \end{aligned} \tag{16}$$

where **u** is the deformation vector of the wing, C is the total compliance of the wing, $\boldsymbol{K}$ is the structural stiffness matrix, $\boldsymbol{f}_a$ is a load vector resulting from the aerodynamic lift force, $\boldsymbol{f}_g$ is the body force loading due to the weight of the wing, N is a load factor (N = 1 for steady level flight), L is the total lift generated by the deformed wing shape, W_b is the weight of the wing box that can change during the optimization (and is dependent on the position of the structural boundary), whereas W_c is the remaining "fixed" weight of the aircraft. Several terms in (16) are dependent on the structural domain, Ω, which is effectively the design variable in the optimization problem. The conventional level set method employs an implicit domain representation, (1), and the objective and constraint functions are implicitly linked to the level-set function. The first constraint in Eq. (16) is the static equilibrium of the aerostructural system and the second constraint is the trim condition. The aerodynamics and pitch-based trim conditions from a tail are not considered for the wing optimization. A ground load taxi-bump case is also considered, where the aerodynamic forces are zero and the trim condition is not enforced.

3.1 Aerodynamic Modeling

The subsonic compressible aerodynamics are modeled using the Doublet Lattice Method (DLM) (Blair 1992; Rodden et al. 1998). The wing planform is divided into discrete boxes, each with a control point at the ¾ chord position. The DLM is used to compute the pressure acting on each box for a given distribution of downwash at the control points:

$$\boldsymbol{D} \cdot \boldsymbol{c}_p = \boldsymbol{w}_c - \alpha \cdot \boldsymbol{z} + \boldsymbol{w}(\boldsymbol{u}) \tag{17}$$

where $\boldsymbol{D}$ is a matrix of non-dimensional aerodynamic influence coefficients and $\boldsymbol{c_p}$ is a vector of differential pressure coefficients for each DLM box, between the upper and lower wing surfaces. There are three sources of downwash at each control point, $\boldsymbol{w_c}$ is the slope of the aerofoil centerline (from built-in camber and twist), α is the angle of attack at the wing root, $\boldsymbol{z}$ is a column vector of ones, and $\boldsymbol{w}(\boldsymbol{u})$ is the additional downwash dependent on the deformed shape of the wing. The total lift force generated by the wing is computed from the DLM box planform areas, the pressure coefficients and the dynamic pressure:

$$L(\boldsymbol{u}) = q \cdot \boldsymbol{a} \cdot \boldsymbol{c}_p = q \cdot \boldsymbol{a}^T \cdot \boldsymbol{D}^{-1} \left\{ \boldsymbol{w}_c - \alpha(\boldsymbol{u}, \Omega) \cdot \boldsymbol{z} + \boldsymbol{w}(\boldsymbol{u}) \right\} \tag{18}$$

where q is the dynamic pressure and $\boldsymbol{a}$ is a column vector containing the DLM box areas.

3.2 Coupling the Structural and Aerodynamic Analyses

The Finite Plate Spline (FPS) method (Appa 1989) is used to communicate information between the FEA and the DLM meshes. A flat plate finite element mesh is constructed between the DLM and FEA discretizations and unit displacement constraints are enforced at locations that coincide with the DLM box centers and a subset of the FEA nodes. Solving the FPS finite element equation under these constraints allows the formulation of two transfer matrices that relate aerodynamic and structural quantities:

$$\boldsymbol{f}_a = q \cdot \boldsymbol{S} \cdot \boldsymbol{c}_p \tag{19}$$

$$\boldsymbol{w}(\boldsymbol{u}) = \boldsymbol{T} \cdot \boldsymbol{u} \tag{20}$$

where $\boldsymbol{S}$ is a matrix that computes the work-equivalent loading on the structure from the pressure coefficients and $\boldsymbol{T}$ is a matrix that converts the structural displacement vector into the downwash component dependent on the deformed wing shape, also in a work-equivalent way. Discrete Kirchoff Triangular (DKT) plate elements (Cook et al. 2002) are used to form the FPS mesh.

Combining the trim condition from Eq. (16) with Eqs. (18) and (20) results in an expression for the required angle of attack for trim in terms of the deformed shape of the wing and current wing box weight:

$$\alpha\left(\boldsymbol{u}, \Omega\right) = \left(L_c + \boldsymbol{b} \cdot \boldsymbol{u} - N \cdot (W_b(\Omega) + W_c) \right) / L_\alpha \tag{21}$$

where L_c and L_α are constants defined as:

$$L_c = q \cdot \boldsymbol{a}^T \cdot \boldsymbol{D}^{-1} \cdot \boldsymbol{w}_c \tag{22}$$

$$L_\alpha = q \cdot \boldsymbol{a}^T \cdot \boldsymbol{D}^{-1} \cdot \boldsymbol{z} \tag{23}$$

and $\boldsymbol{b}^T$ is a constant vector defined as:

$$\boldsymbol{b}^T = q \cdot \boldsymbol{a}^T \cdot \boldsymbol{D}^{-1} \cdot \boldsymbol{T} \tag{24}$$

The matrices $\boldsymbol{S}$ and $\boldsymbol{T}$ allow information to pass between the DLM and FEA and they can also be used to formulate an aerodynamic stiffness matrix:

$$\boldsymbol{Q} = q \cdot \boldsymbol{S} \cdot \boldsymbol{D}^{-1} \cdot \boldsymbol{T} \tag{25}$$

Note that the $\boldsymbol{Q}$ matrix is constant for a given wing planform and flight condition, defined by velocity, air density and Mach number. However, the Mach number dependence is contained within $\boldsymbol{D}$, whereas velocity and air density are used to define q. Thus, if the Mach number is changed, then the $\boldsymbol{D}$ matrix has to be recomputed and inverted to update the $\boldsymbol{Q}$ matrix. If dynamic pressure is changed then the update of $\boldsymbol{Q}$ only involves a scalar multiplication of $\boldsymbol{Q}$. The aerodynamic load vector in Eq. (16) can be computed from Eqs. (17), (19) and (25):

$$\boldsymbol{f}_a(\boldsymbol{u},\Omega) = \boldsymbol{f}_c - \alpha(\boldsymbol{u},\Omega) \cdot \boldsymbol{f}_\alpha + \boldsymbol{Q} \cdot \boldsymbol{u} \tag{26}$$

where $\alpha(\boldsymbol{u})$ is defined by Eq. (21), $\boldsymbol{f}_c$ and $\boldsymbol{f}_\alpha$ are constant load vectors defined as:

$$\boldsymbol{f}_c = q \cdot \boldsymbol{S} \cdot \boldsymbol{D}^{-1} \cdot \boldsymbol{w}_c \tag{27}$$

$$\boldsymbol{f}_\alpha = q \cdot \boldsymbol{S} \cdot \boldsymbol{D}^{-1} \cdot \boldsymbol{z} \tag{28}$$

The trim condition in Eq. (16) can now be eliminated and the problem re-stated as:

$$\begin{aligned} &\underset{\Omega}{\text{Minimize:}}\ C(\boldsymbol{u},\Omega) = \boldsymbol{f}_t(\boldsymbol{u},\Omega) \cdot \boldsymbol{u} \\ &\text{Subject to:}\ \boldsymbol{K}(\Omega) \cdot u = \boldsymbol{f}_t(\boldsymbol{u},\Omega) = \boldsymbol{f}_a(\boldsymbol{u},\Omega) + N \cdot \boldsymbol{f}_g(\Omega) \end{aligned} \tag{29}$$

where the aerodynamic load vector $\boldsymbol{f}_a(\boldsymbol{u}, \Omega)$ is defined by Eq. (26) and the required angle of attack for trim is defined by Eq. (21). The only constraint in Eq. (29) is the static equilibrium equation for the coupled aerostructural system, which is implicitly satisfied when solving for $\boldsymbol{u}$. Thus, the optimization problem defined in Eq. (29) can be solved using unconstrained methods, although it may be necessary to introduce an upper limit on the structural volume to obtain useful results. For compliance minimization problems without design dependent loading a volume constraint is necessary to prevent the trivial solution where the design domain is completely filled with material. A volume constraint is not required here, as adding weight to the wing can increase the compliance because of the design dependent loads. Adding weight will increase the aerodynamic loads, through an increase angle of attack for trim, and also increase the body force loads. Also, the DLM cannot model stalled flow. However, this effect is not considered in this work and a constraint on the angle of attack is not used.

The complete approach to the coupled aerostructural analysis is summarized in Table 1.

Table 1. Summary of the coupled aerostructural analysis.

Method	Equations	Description	Reference
FEA	$\boldsymbol{K}\cdot\boldsymbol{u} = \boldsymbol{f}_a(\boldsymbol{u}) + N\cdot\boldsymbol{f}_g$	Structural analysis. 8 node tri-linear elements with incompatible modes.	Cook et al. (2002)
DLM	$\boldsymbol{D}\cdot\boldsymbol{c}_p = \boldsymbol{w}_c - \alpha\cdot\boldsymbol{z} + \boldsymbol{w}(\boldsymbol{u})$	Panel method for subsonic, compressible aerodynamic analysis.	Blair (1992) Rodden et al. (1998)
FPS	$\boldsymbol{f}_a = q\cdot\boldsymbol{S}\cdot\boldsymbol{c}_p$ $\boldsymbol{w}(\boldsymbol{u}) = \boldsymbol{T}\cdot\boldsymbol{u}$	Coupling matrices $\boldsymbol{S}$ and $\boldsymbol{T}$ derived from a plate FEA with displacemt constraints at coupling points.	Appa (1989)

3.3 Shape Sensitivity Analysis

Until now we have formulated the governing equations and compliance function in discrete forms, which are really discretizations of the continuous equations. To obtain the shape derivative for the problem defined in Eq. (29) using the results from Allaire et al. (2004) the continuous forms are used. The compliance can be written in a continuous form as:

$$C(\Omega,u) = N\int_\Omega (f_g\cdot u)d\Omega + \int_{\Gamma_N}(f_c\cdot u)d\Gamma_N - \alpha(u,\Omega)\int_{\Gamma_N}(f_a\cdot u)\,d\Gamma_N + \int_{\Gamma_N}(Q_{i,j}u_i\cdot u_j)\,d\Gamma_N \quad (30)$$

where Γ_N is the part of the boundary where the aerodynamic loads are applied (such as the upper surface of the wing) and $Q_{i,j}$ is the continuous tensor form of the aerodynamic stiffness. The continuous form of the aerostructural equilibrium equation is:

$$\begin{aligned}\int_\Omega (E\varepsilon(u)\cdot\varepsilon(v))d\Omega = N\int_\Omega (f_g\cdot v)d\Omega + \int_{\Gamma_N}(f_c\cdot v)d\Gamma_N - \alpha(u,\Omega)\int_{\Gamma_N}(f_a\cdot v)\,d\Gamma_N \\ + \int_{\Gamma_N}(Q_{i,j}v_i\cdot u_j)\,d\Gamma_N + \int_{\Gamma_D}(v\cdot E\varepsilon(u)n + u\cdot E\varepsilon(v)n)\,d\Gamma_D\end{aligned} \quad (31)$$

where E is the material property tensor, $\varepsilon(u)$ is the strain tensor, v is a virtual displacement, n is a unit vector normal to the boundary and Γ_D is the part of the boundary where displacement boundary conditions are applied.

The adjoint method is used to obtain the shape derivative of Eq. (30). First, a Lagrangian function is formed by adding the aerostructural equilibrium equation, Eq. (31), to the objective, Eq. (30), using a Lagrange multiplier, λ:

$$\begin{aligned}\Lambda(\Omega,v,\lambda) = C(\Omega,v) - \int_\Omega (E\varepsilon(v)\cdot\varepsilon(\lambda))d\Omega + N\int_\Omega(\lambda\cdot f_g)d\Omega + \int_{\Gamma_N}(\lambda\cdot f_c)d\Gamma_N \\ - \alpha(v,\Omega)\int_{\Gamma_N}(\lambda\cdot f_\alpha)\,d\Gamma_N + \int_{\Gamma_N}(Q_{i,j}\lambda_i\cdot v_j)\,d\Gamma_N + \int_{\Gamma_D}(\lambda\cdot E\varepsilon(v)n + v\cdot E\varepsilon(\lambda)n)\,d\Gamma_D\end{aligned} \quad (32)$$

The adjoint equation is derived by differentiating Eq. (32) with respect to v in the direction θ and defining (u, p) as a stationary point, where θ is an arbitrary vector. After collecting similar terms:

$$\left\langle \frac{\partial \Lambda}{\partial v}(\Omega,u,p),\theta \right\rangle = 0 = N\int_{\Omega}\left(f_g\cdot\theta\right)d\Omega + \int_{\Gamma_N}\left(f_a(u)\cdot\theta\right)d\Gamma_N - \frac{\partial\alpha(u,\Omega)}{\partial u}\int_{\Gamma_N}\left(f_\alpha\cdot(u+p)\right)\theta\, d\Gamma_N$$
$$+\int_{\Gamma_N}\left(Q_{i,j}(u_i+p_i)\cdot\theta_j\right)d\Gamma_N - \int_{\Omega}\left(E\varepsilon(\theta)\cdot\varepsilon(p)\right)d\Omega + \int_{\Gamma_D}\left(p\cdot E\varepsilon(\theta)n + \theta\cdot E\varepsilon(p)n\right)d\Gamma_D \tag{33}$$

where the chevron brackets denote a vector inner product. To complete the derivative in Eq. (33) the change in angle of attack due to a change in deformed wing shape is required. From Eq. (21):

$$\partial\alpha(u,\Omega)/\partial u = \boldsymbol{b}/L_\alpha \tag{34}$$

Using FEA to solve the adjoint equation, Eq. (33) can be written in the following discrete matrix form:

$$\boldsymbol{K}^T\cdot\boldsymbol{p} = N\cdot\boldsymbol{f_g} + \boldsymbol{f_a}(\boldsymbol{u}) + \left[\boldsymbol{Q}^T - \left(\boldsymbol{b}\otimes\boldsymbol{f}_\alpha\right)/L_\alpha\right]\left(\boldsymbol{u}+\boldsymbol{p}\right),\ \ u = p = 0 \text{ on } \Gamma_D \tag{35}$$

The shape derivative can now be computed by differentiating the Lagrangian, Eq. (32) with respect to the shape in the direction θ, at the stationary point (u, p). During optimization, the part of the boundary where boundary conditions and aerodynamic loads are applied is fixed, thus $\theta = 0$ on these parts and we only compute the shape derivative on the remaining free part of the boundary, Γ_0:

$$\frac{\partial\Lambda}{\partial\Omega}(\Omega,u,p)(\theta) = \int_{\Gamma_0}\theta\cdot n\left(N\cdot f_a\cdot(u+p) - E\varepsilon(u)\cdot\varepsilon(p)\right)d\Gamma_0 - \frac{\partial\alpha(u,\Omega)}{\partial\Omega}\int_{\Gamma_N}\left(f_\alpha\cdot(u+p)\right)d\Gamma_N \tag{36}$$

The second term on the right hand side of Eq. (36) is the change in the compliance with respect to a change in the angle of attack due to a change in the total weight of the structure. Thus, from Eq. (21) the derivative of α with respect to the shape, at the stationary point, is simply the shape derivative of the structural weight multiplied by the load factor over L_α:

$$\partial\alpha(u,\Omega)/\partial\Omega = -N/L_\alpha\int_{\Gamma_0}\theta\cdot n\left(\rho g\right)d\Gamma_0 \tag{37}$$

where ρ is the density of the material and g is acceleration due to gravity. Setting $\theta\cdot n$ equal to the normal velocity, where a positive velocity is an inward movement: $\theta\cdot n = -V_n$, the final shape derivative on the free boundary becomes:

$$\frac{\partial C}{\partial\Omega}(\Omega,u,p) = \int_{\Gamma_0}V_n\left(E\varepsilon(u)\cdot\varepsilon(p) - N\cdot f_a\cdot(u+p) - A\cdot\rho g\right)d\Gamma_0,\ \ A = \frac{N}{L_\alpha}\int_{\Gamma_N}\left(f_\alpha\cdot(u+p)\right)d\Gamma_N \tag{38}$$

where A is a factor, constant over the entire boundary, that relates the change in compliance due to a change in the angle of attack, resulting from a change in the wing box weight.

To solve the aerostructural optimization problem stated in Eq. (29) using the level set method, the shape derivative must be negative to ensure a decrease in the objective. Thus, the velocity function is defined such that the shape derivative, Eq. (38) is negative everywhere on the free boundary. The velocity function is simply defined as:

$$V_n = N \cdot f_g \cdot (u + p) + A \cdot \rho g - E\varepsilon(u)\varepsilon(p) \tag{39}$$

This velocity function is used with the level set method described in Section 2 to progressively improve the structure with respect to the optimization objective. The sensitivity calculation was validated against sensitivities obtained using finite differences.

3.4 Solution of the Primary and Adjoint Aerostructural Problems

The aerodynamic load vector is a linear function of the structural displacement, which can be seen by substituting equations (21), (27) and (28) into (26). Therefore, the aerostructural equilibrium equation (29) can be restated as a linear equation and solved directly. However, in practice this may not be an efficient approach, as the aerodynamic stiffness matrix is dense, whereas the structural stiffness matrix is sparse. Methods employed to efficiently solve static linear elastic equations may not be efficient for solving the coupled equation, due to the dense matrix. Therefore, it can be more efficient to use an iterative approach to solve the aerostructural equilibrium equation.

The iterative approach employed in this work starts with a load vector computed assuming no coupling between the aerodynamic loads and deformed wing shape. The deformed wing shape is obtained for the current load vector, which is then used to update the load vector by including the coupling terms. This process is repeated until the difference between the previous and updated load vectors is very small. The process can be summarized as:

1. Initialize load vector: $\boldsymbol{f}^0 = N \cdot \boldsymbol{f_g} + \boldsymbol{f_a}(\boldsymbol{0})$
2. Solve: $\boldsymbol{K} \cdot \boldsymbol{u}^{k+1} = \boldsymbol{f}^k$
3. Update load vector: $\boldsymbol{f}^{k+1} = N \cdot \boldsymbol{f_g} + \boldsymbol{f_a}(\boldsymbol{u}^{k+1})$
4. Check for convergence: $\| \boldsymbol{f}^{k+1} - \boldsymbol{f}^k \| < small$

The iterative approach has been shown to be efficient, although it can be unstable and fail to converge, especially for more flexible wings. To overcome this, a non-converging solution is detected by tracking the difference in subsequent load vectors. Specifically, if $\| \boldsymbol{f}^{k+1} - \boldsymbol{f}^k \| > \| \boldsymbol{f}^k - \boldsymbol{f}^{k-1} \|$ then the solution is non-converging and an under-relaxation approach is used to obtain the next load vector: $\boldsymbol{f}^{k+1} = N \cdot \boldsymbol{f_g} + 0.25\, \boldsymbol{f_a}(\boldsymbol{u}^k) + 0.75\, \boldsymbol{f_a}(\boldsymbol{u}^{k-1})$. The relaxation factor of 0.25 was chosen to give a good compromise between efficiency and stability for the examples studied in this work.

The iterative approach is also used to solve the adjoint equation, Eq.(35). In this case the displacement vector, $\boldsymbol{u}$, is known from the solution of the primary equation. The initial adjoint load vector is computed using: $\boldsymbol{p} = 0$. The adjoint solution is then obtained using the same iterative approach that is used to find the primary solution, including the under-relaxation method for stabilization.

4. Optimization of a CRM Wing Box

The 3D unstructured mesh level set method, detailed in Section 2, is used to solve the aerostructural optimization problem, detailed in Section 3. The subject of the optimization is the internal configuration of the CRM wing box (Vassberg et al. 2008).

4.1 The Common Research Model Wing

The CRM is a transonic transport configuration with an aspect ratio of 9, a taper ratio of 0.275, a sweep angle of 35°, and a cruise Mach number of 0.85. For all flight loads a dynamic pressure of 5,897 Pa is used. The wing box is located between 12% and 71% of the local airfoil chord. The fixed weight of the aircraft is 500 kN, thus, in steady level flight, each wing must produce enough lift to support 250 kN plus the weight of one wing. The wing box structure is made from aluminum, with a Young's modulus of 68.95 GPa, Poisson's ratio of 0.3 and density of 2800 kg/m^3.

The CRM wing box mesh is shown in Fig. 7 and has 150,300 hexahedral elements and 166,160 nodes. There are 15 elements though the depth, 30 along the chord and 334 along the span. This mesh is used for the FEA and to discretize the implicit level set function. All degrees of freedom for nodes at the wing root are fixed. The DLM mesh is composed of 20 × 100 boxes in the chord-wise and span-wise directions, respectively, Fig. 8. The FPS method is used to apply the aerodynamic loads to a subset of 1705 nodes on the upper surface of the structural mesh, Fig. 9. When the FPS method is used to transform displacements into downwash, Eq. (20), the average of upper and lower skin displacements is used. The complete aeroelastic model, described in Section 3, was validated against results obtained from NASTRAN. FEA and DLM results were validated independently, before validating the complete model, including the FPS method.

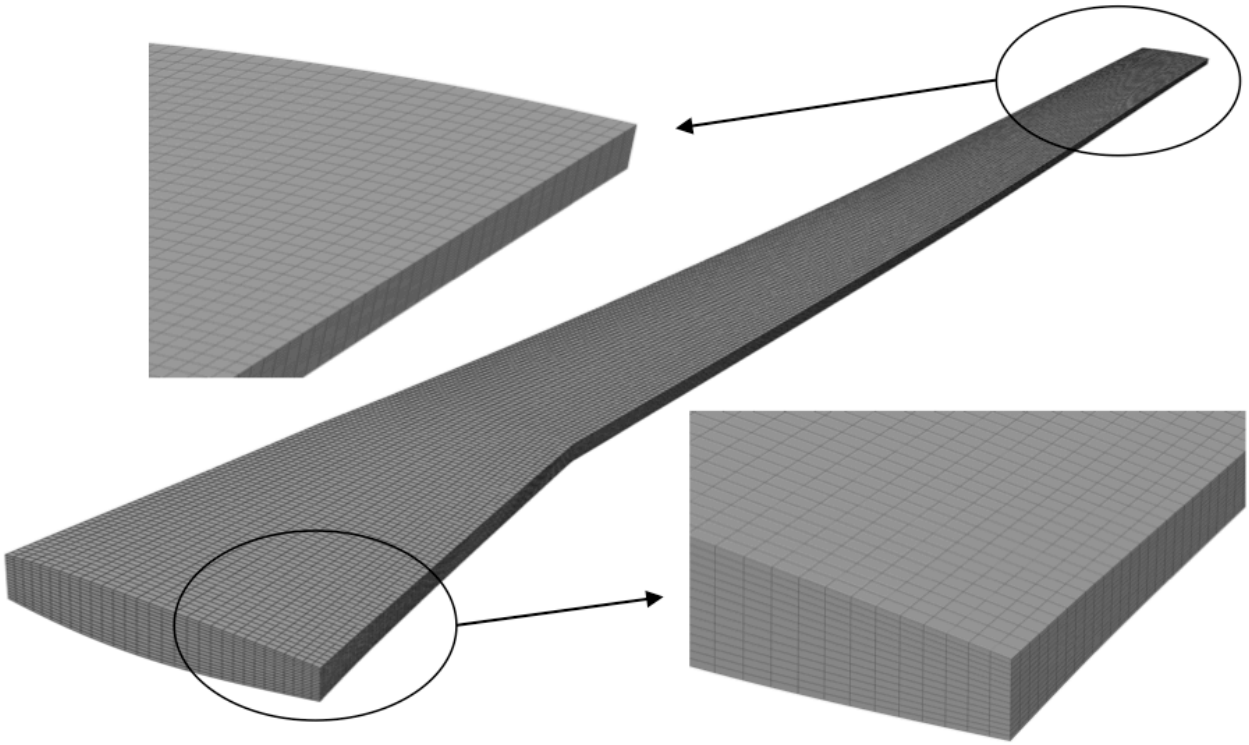

Figure 7. CRM solid wing box mesh.

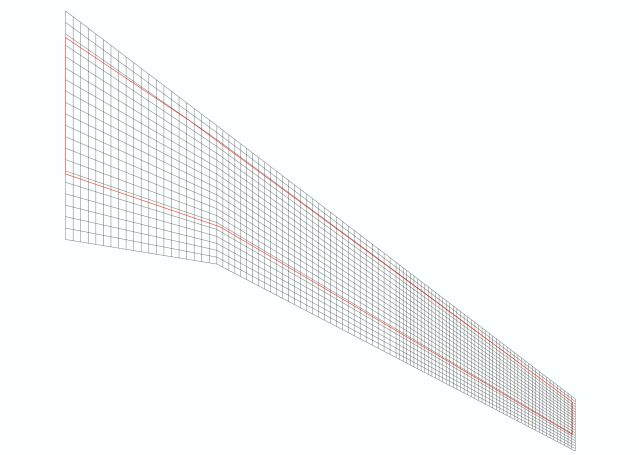

Figure 8. DLM mesh (CRM wing box outlined in red).

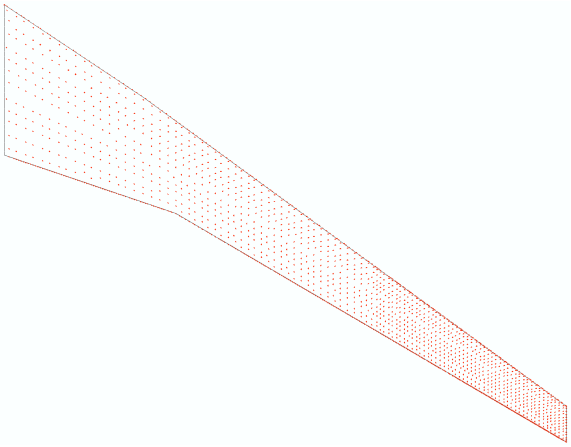

Figure 9. Down selected nodes used in the FPS method.

The hexahedra finite elements used to discretize the wing box cannot model thin, shell-like structures typical of the conventional semi-monocoque configuration. Therefore, the structures obtained using the mesh in Fig. 7 are likely to be heavier than real wing boxes. This will result in a high angle of attack and large body force loads, which would make comparison to conventional configurations difficult. To obtain reasonable topologies with the mesh in Fig. 7, the modulus and density of the material used during the entire optimization are 10% of the real values, which are 6.895 GPa and 280 kg/m^3, respectively.

The 3D level set optimization method is free to choose any structure within the wing box domain and is not restricted by any predefined configuration. However, during the optimization a single layer of elements on the outer surface of the design domain is fixed to remain part of the structure. This includes the upper and lower surfaces and all sides of the wing box. The upper and lower layers of elements then act as the upper and lower skins. This ensures that holes do not develop in the upper and lower skins and that the skins remain connected. Finally the convergence criterion used for all examples is $\gamma = 10^{-3}$, Eq. (15). This value was chosen based on the observed convergent behavior of the examples studied in this work.

4.2 Single Load Case

This section considers several single load case problems for a range of loading conditions, including flight maneuvers, characterized by the load factor, N, and a ground load case, which is a 2.5g taxi-bump. The ground load case only considers static body force loads and does not consider any aerodynamic loading or the trim condition. The initial configuration in each case is shown in Fig. 10, where material fills the wing box with regularly distributed spherical voids. The initial voids are required, as the current method cannot automatically create new holes during optimization.

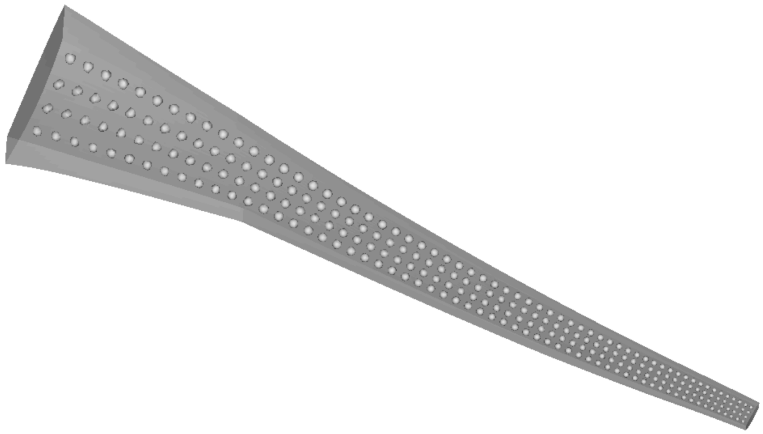

Figure 10. CRM wing box initial design.

4.2.1 Steady level flight

The first single load case problem is steady level flight with a load factor: $N = 1$. The solution is shown in Fig. 11 Solutions are shown as a 3D contour of the internal topology and the design domain is also shown in darker grey. Some solutions are also shown using 2D slices though the topology. The topology of the solution is relatively simple, as material is added to the outboard region and removed from the inboard region, although there are some subtle variations of the skin thickness in the inboard area. The extra material towards the tip helps reduce compliance by inertia relief, as the increase in the body force loading outboard acts to oppose the wing bending caused by the aerodynamic lift. The material removed from the inboard region also helps reduce compliance, as the wing box weight is reduced, which results in a reduced angle of attack and reduced aerodynamic loading. This is shown is Fig. 12, where the angle of attack reduces with the weight of the wing-box due to the trim condition that lift equals weight. The two primary factors driving the topology in this case appear to be an increase of body force loading outboard and an overall weight reduction to reduce the root angle of attack and associated loading. There are some subtle variations of the skin thickness, which are suggestive of stringers. These features appear to perform some aeroelastic tailoring, as the angled reinforcement induces a bend-twist coupling under aerodynamic loading. The unstructured 3D level set method performed well and the solution converged smoothly in 47 iterations, Fig. 13.

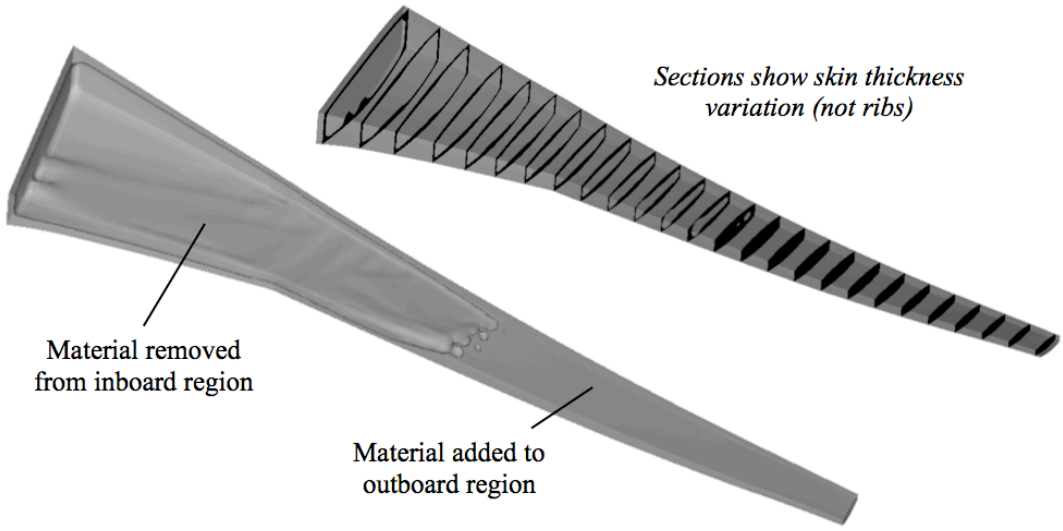

Figure 11. Steady level flight solution.

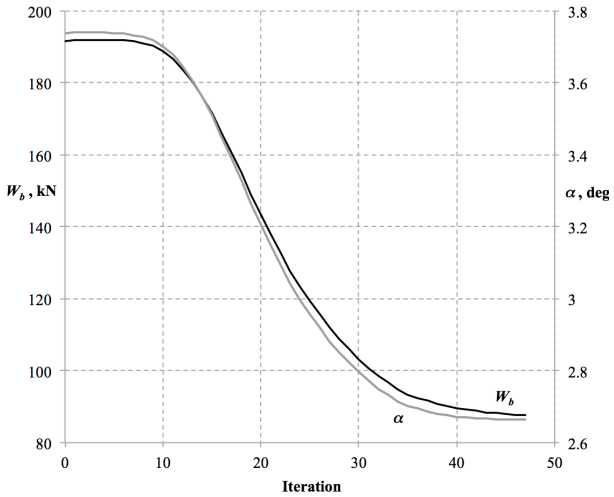

Figure 12. Steady level flight, weight and angle of attack.

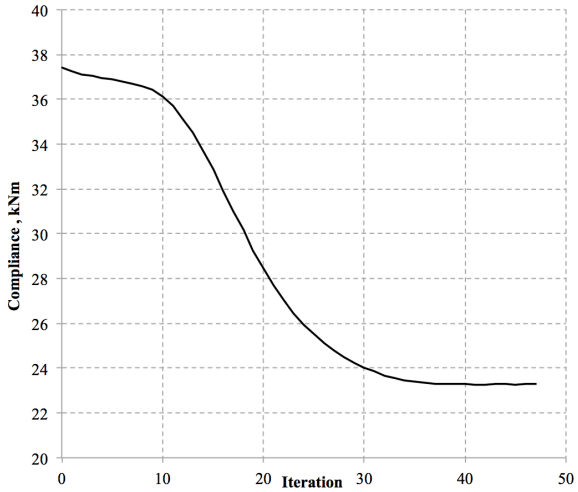

Figure 13. Steady level flight, compliance.

4.2.2 Dependence on loading

To investigate the dependence of the steady level flight solution on the applied loading, the optimization is repeated without the self-weight body force loading. This removes the inertia relief effect that is a significant factor driving the optimal topology seen in Fig. 11.

In addition, the effect of including the aeroelastic coupling during the optimization is investigated by solving the minimization of compliance problem with uncoupled, fixed aerodynamic loading and a fixed angle of attack. The aeroelastic coupling, trim condition and body forces are not included. For this problem, a constraint on the maximum volume is required to prevent the trivial solution of a solid wing filled with material. The angle of attack is fixed at 2.5° and the volume constraint is set to 40% of the total wing box volume, which is equal to a weight of 78.64 kN under a 1g load. For comparison, the volume fraction for the solution in Fig. 11 is 44.6%. The volume constraint is handled by the Sequential Linear Programming (SLP) level set method (Dunning and Kim 2014). This method uses discretized boundary surface integrals to compute the constraint change for a given velocity function. The method of subdividing elements into simplexes (tetrahedra in 3D) is used to perform the boundary surface integration for the 3D unstructured mesh (Min and Gibou 2007). The solutions for the no self-weight and no aeroelastic coupling problems are shown in Fig. 14.

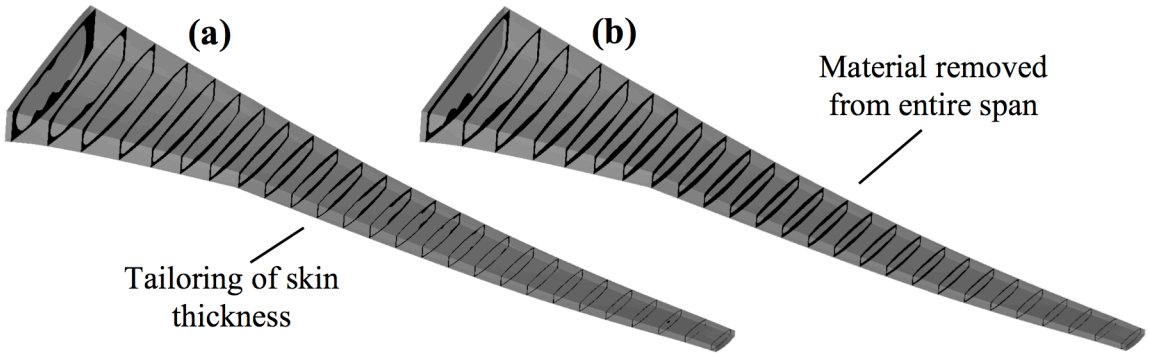

Figure 14. Steady level flight: a) No self-weight, b) No aeroelastic coupling. Sections show skin thickness (not ribs).

Both solutions in Fig. 14 have material removed along the entire span of the wing. There are no body forces applied, so the optimizer cannot take advantage of the inertia relief effect, thus material is not added to the outboard region. For the no self-weight solution, Fig 14a, material is removed from the inboard section to reduce the total weight, required angle of attack for trim and total aerodynamic loading. However, inboard material removal for the solution obtained without aeroelastic coupling, Fig 14b, is simply driven by the volume constraint, which is active at the optimum. Although the two solutions are similar, the solution obtained with aeroelastic coupling has noticeably more tailoring of the skin thickness, particularly in the central span-wise region of the wing. This is an aeroelastic tailoring effect, as the forward sweep of the skin thickness in Fig. 14a rotates the elastic axis forward, leading to increase of the natural wash-out of the back-swept wing under aerodynamic loading. This reduces the angle of attack and loading outboard, which helps reduce the compliance of the cantilevered wing under aerodynamic loads. To investigate this effect further, the solution obtained without aeroelastic coupling is analyzed with the

aeroelastic coupling turned on. The compliance obtained in this case is 39.5 kNm, compared with 36.7 kNm for the solution that uses aeroelastic coupling throughout the optimization, Fig 14a. This highlights the importance of including the aeroelastic coupling for wing structure optimization.

4.2.3 Flight maneuvers

Two flight maneuvers are considered, a pull-up maneuver, with N = 2.5, and a push-over maneuver, with N = -1. These were chosen as they are typically used to size an aircraft at the boundaries of the flight envelope (Niu 1988). All other parameters are the same as for the steady level flight example. The solutions for the pull-up and push-over maneuvers are shown in Fig. 15. The topologies for the maneuver cases are very similar to the solution for the steady level flight case, Fig. 11, with only small differences in the thickness of the skins. This is not surprising, as the two main factors that drive the topology are the body force loading and aerodynamic loading from the root angle of attack, both of which scale linearly with the load factor. The results for the flight load cases are not exactly the same, noting the small differences in the skin thickness variations, as the constant part of the aerodynamic load vector from built in camber and twist does not vary with the load factor.

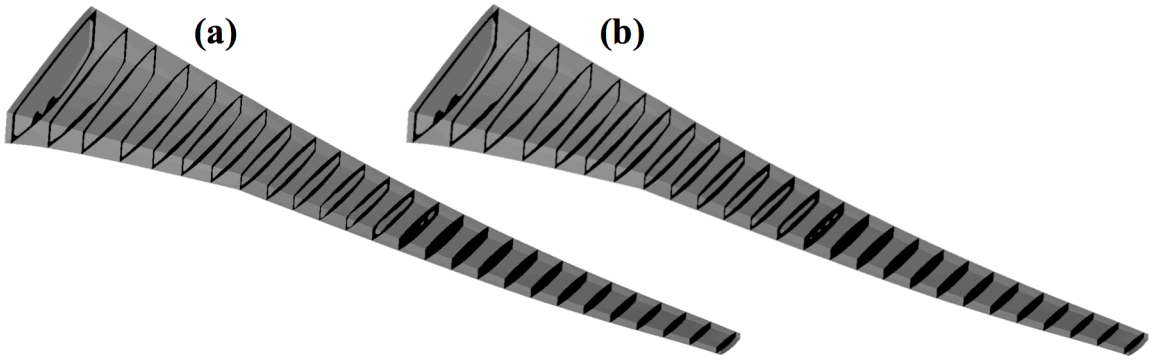

Figure 15. Solutions for flight maneuvers: a) Pull-up, N = 2.5, b) Push-over, N = -1. Sections show skin thickness (not ribs).

4.2.4 Taxi-bump

The optimal solutions for the flight load cases that consider body forces have a concentration of material at the tip for inertia relief, Figs 11 & 15. This is undesirable when considering some ground load cases, such as the taxi-bump case, as the moment due to the tip mass can exceed that caused by the flight loads (Wakayama and Kroo 1995). The load factor for the taxi-bump case is N = -2.5. No aerodynamic loads are applied and the trim condition is not enforced. The taxi-bump case is self-adjoint, as the adjoint equation, Eq. (35), reduces to the static equilibrium equation, thus $u = p$. The solution for the taxi-bump case is shown in Fig. 16 and is very different from the flight load case solutions in Figs 11 & 15. Material has been removed from the outboard region to reduce the inertia effect on the bending and some material has been added to the inboard region, to reinforce the wing box against bending. Some initial voids in the inboard region persist, which suggests that the removal of these voids has little impact on the compliance, compared with the convergence tolerance. Another difference from the flight load solutions is the lack of local variations in the wing skin thickness, which further supports the idea that this feature is a result of the aeroelastic coupling for the flight load examples.

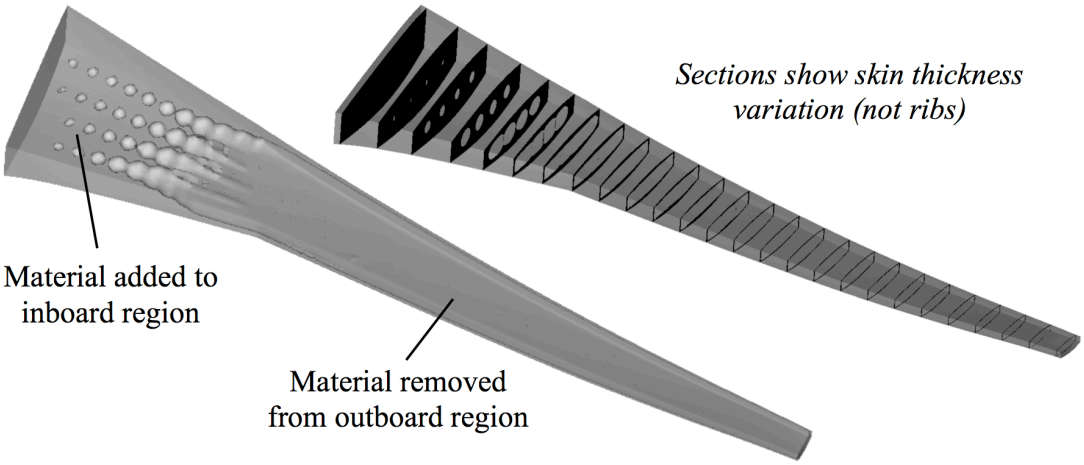

Figure 16. Taxi-bump solution.

4.3 Multiple Load Cases

The results in the previous section show that optimal designs for flight load cases with body-force loads have a concentration of material in the outboard region for inertia relief, Figs. 11 and 15. This feature is undesirable for ground load cases and the optimal design for the taxi-bump case has minimal material outboard, Fig. 16. Therefore, the optimal designs for flight load and ground load cases are conflicting. The trade-off between these two load cases is explored by solving a multiple load case problem where one load case is steady level flight and the second load case is the taxi-bump:

$$\text{Minimize: } \eta C_f + \left(1-\eta\right) C_g \tag{40}$$

where C_f is the compliance from the steady level flight case, C_g is the compliance from the ground load taxi-bump case and η is a weighting factor for the two cases, where $\eta \in [0,1]$. The shape derivative for the multiple load case problem is simply the weighted sum of the derivatives from each case.

The multiple load case problem, Eq. (40), was solved for five values of η : 0.0, 0.25, 0.5, 0.75, 1.0. The solution for η = 1.0 is the same as the steady level flight solution, Fig. 11, and the solution for η = 0.0 is the same as the taxi-bump solution, Fig. 16. Solutions for the other η values are shown in Fig. 17. Table 2 shows a summary of wing box weight values and compliance values, for each solution and both load cases, as expected the compliance for the flight load case increases with decreasing η and the opposite occurs for the ground load compliance. However, the trend for wing box weight is unclear.

Table 2. Multiple load cases, compliance and wing box weight values.

η	C_f , kNm	C_g , kNm	W_b , kN
1.00	23.3	38.5	87.7
0.75	28.3	6.0	64.3
0.50	29.9	3.2	59.9
0.25	31.4	2.7	60.4
0.00	47.8	2.2	119.3

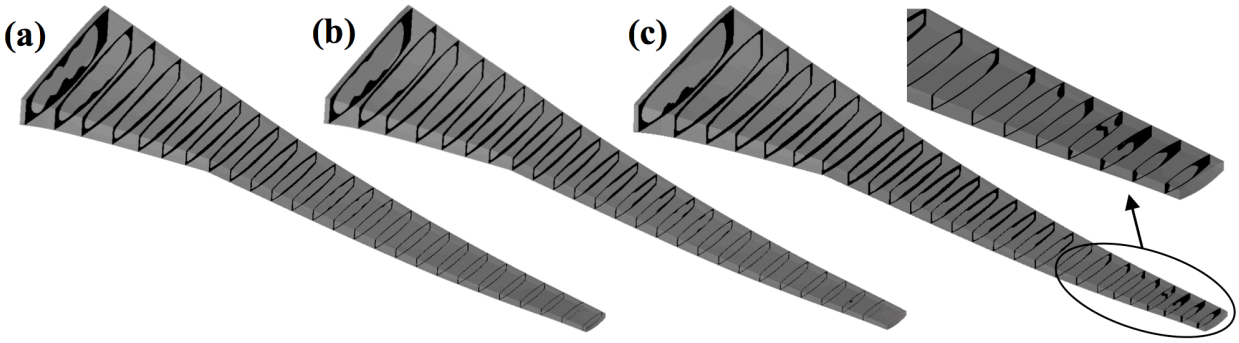

Figure 17. Multiple load case solutions: a) η = 0.25, b) η = 0.5, c) η = 0.75. Sections show skin thickness (not ribs).

All of the multiple load case solutions have material removed from the entire span of the wing, Fig. 17. This results in wing box designs with significantly lower weight than either of the single load case optima, Table 2. The taxi-bump load case penalizes the inertia relief effect seen in the flight load case optimum designs, leading to the removal of outboard material. In contrast, the flight load case drives the optimizer to remove inboard material to reduce the angle of attack for trim. The flight load case also optimizes the skin thickness variation, which is likely an aeroelastic tailoring effect. Therefore, the multiple load case approach seems to be an effective method of obtaining stiff wing designs for both flight and ground load cases.

Although the multiple load case optima are similar, the choice of η value does affect the solution and there are some differences in the designs. The most noticeable are for the solution obtained using η = 0.75, where a significant amount of material is retained in the tip leading edge region. A detailed view of this design using a series of cross sections is shown in Fig. 17c. The skin thickness near the trailing edge reduces in the outboard region, whereas a significant amount of material is retained in the tip leading edge region. The extra material at the tip provides inertia relief for the flight load case, although less material is added compared with the solution for pure flight loads (Fig. 11) as tip mass is penalized by the taxi-bump load case. The increase of skin thickness towards the leading edge also locally moves the elastic axis forwards. This is an aeroelastic tailoring effect, as the natural wash-out of the back swept wing is increased (Niu 1988), leading to a reduced angle of attack outboard and hence the load distribution is moved inboard. Moving the load distribution inboard is desirable for compliance optimization and wing structure design in general, as the overall bending moment on the wing is reduced. In fact, the magnitude of root bending moment computed from the aerodynamic loading, with an angle of attack of 2.5°, is 34% lower for the η = 0.75 solution, compared with the η = 0.50 solution.

The wing box structures obtained in this work using a 3D level set topology optimization method are very different from conventional structures. There are no internal spar or rib members and the topologies mainly consist of large volumes that are either void or filled with material. The level set optimization method seems to focus mainly on reinforcement of the fixed part of the wing box structure, namely the outer layer of elements representing the skins and what can be described as front and rear spars.

The optimal designs obtained here could provide a starting point for more detailed design, including consideration for manufacturability. Alternatively, optimum designs obtained using level set topology optimization may be realized with little modification by utilizing additive manufacturing techniques, such as EBF^3 (Taminger and Hafley 2003).

5. Conclusions

This paper develops a conventional level set based optimization method applicable to 3D unstructured meshes. The method employs the fast marching method for efficient velocity extension and re-initialization and an upwind scheme to solve the H-J equation. Numerical procedures are developed to make the fast marching method robust for unstructured meshes, such as checking for upwind validity and backtracking.

The level set optimization method is applied to design the wing box structure of the NASA Common Research Model, where the optimizer is free to choose any structure within the 3D wing box space. The compliance of the wing box is minimized under body force and aerodynamic loading, which is coupled to the deformed wing shape. The root angle of attack is allowed to change during the optimization to meet the trim condition that weight equals lift. The adjoint method is used to obtain the shape derivative of the coupled aerostructural problem, which is then used to define the velocity function for the level set method.

The compliance minimization problem is solved for single load cases, including steady level flight, maneuvers and a ground load taxi-bump case. The solutions are remarkably different from conventional rib/spar type designs, as the topologies mostly consist of large volumes that are either void or filled with material and the optimizer mainly adds reinforcement to the fixed parts of the structure. However, it is known that solutions obtained using the level set method and the convergence behavior may be dependent on the initial distribution of voids. This needs to be further investigated for the method and examples presented in this paper.

The solutions for the flight load cases are very similar, with material added to the outboard region for inertia relief. In contrast, the solution for the taxi-bump case removed material from the outboard region to reduce the inertia loading effect. To resolve this conflict in optimal designs for flight and ground load cases, a multiple load case problem is formulated, where one case is steady level flight and the other is the taxi-bump. This approach provides reasonable compromise solutions for good flight and ground load performance. The effects of the self-weight loading and aeroelastic coupling were also investigated, showing how they influence the optimal design.

The 3D unstructured mesh level set method developed in this paper is able to efficiently and smoothly obtain solutions for the compliance minimization of the CRM wing box. Therefore, the method is promising for general applications of conventional level set optimization to problems with arbitrary shaped domains.

Acknowledgements
This work is funded by the Fixed Wing project under the National Aeronautics and Space Administration's (NASA) Fundamental Aeronautics Program. The authors would like to thank Dr. Maxwell Blair for his example DLM code and the Numerical Analysis Group at the Rutherford Appleton Laboratory for their FORTRAN HSL packages (HSL, a collection of Fortran codes for large-scale scientific computation. See http://www.hsl.rl.ac.uk/).

References:

Allaire G, Jouve F, Toader A (2004) Structural optimization using sensitivity analysis and a level-set method. Journal of Computational Physics 194(1):363–393.

Allaire G, de Gournay F, Jouve F, Toader A (2005) Structural optimization using topological and shape sensitivity via a level set method. Control Cybern 34(1):59-80.

Appa K (1989) Finite-Surface Spline. Journal of Aircraft 26(5):495-496.

Balabanov VO, Haftka RT (1996) Topology optimization of transport wing internal structure. Journal of Aircraft 33(1):232-233.

Bendsøe MP, Sigmund O (2004) Topology optimization: Theory, Methods and Applications. Springer-Verlag, Germany.

Blair M (1992) A compilation of the mathematics leading to the doublet lattice method. Report No. WL-TR-92-3028, Wright-Patterson Air Force Base, Ohio.

Brampton CJ, Kim HA, Cunningham JL (2012) Level set topology optimisation of aircraft wing considering aerostructural interaction. 14th AIAA/ISSMO Multidisciplinary Analysis and Optimization, Indianapolis, IN USA, Sept.

De Leon DM, de Souza CE, Fonseca JSO, da Silva RGA (2012) Aeroelastic tailoring using fiber orientation and topology optimization. Structural and Multidisciplinary Optimization 46(5):663-677.

Cook R, Malkus D, Plesha M, Witt R (2002) Concepts and Applications of Finite Element Analysis, 4th ed., John Wiley & Sons, New York.

Deaton JD, Grandhi RV (2014) A survey of structural and multidisciplinary continuum topology optimization: post 2000. Structural and Multidisciplinary Optimization 49(1):1-38.

Dunning PD, Brampton CJ, Kim HA (2013) Multidisciplinary level set topology optimization of the internal structure of an aircraft wing. 10th World Congress on Structural and Multidisciplinary Optimization, Orlando, Florida, USA, May 19-24.

Dunning PD, Kim HA, Mullineux G (2011) Investigation and improvement of sensitivity computation using the area-fraction weighted fixed grid FEM and structural optimization. Finite Elements in Analysis and Design 47(8):933-941.

Dunning PD, Kim HA (2013) A new hole insertion method for level set based structural topology optimization. International Journal for Numerical Methods in Engineering 93(1):118-134.

Dunning PD, Kim HA (2014) Introducing the sequential linear programming level-set method for topology optimization. Structural and Multidisciplinary Optimization (Accepted). Doi: 10.1007/s00158-014-1174-z.

Eschenauer HA, Olhoff N (2001) Topology optimization of continuum structures: a review. Applied Mechanics Reviews 54(4):331-390.

Eves J, Toropov VV, Thompson HM, Gaskell PH, Doherty JJ, Harris JC "Topology Optimization of Aircraft with Non-Conventional Configurations," 8th World Congress on Structural and Multidisciplinary Optimization, Lisbon, Portugal, June 1-5, 2009.

Gain AL, Paulino GH (2013) A critical comparative assessment of differential equation-driven methods for structural topology optimization. Structural and Multidisciplinary Optimization 48(4):685-710.

Gomes AA, Suleman A (2008) Topology optimization of a reinforced wing box for enhanced roll maneuvers. AIAA Journal 46(3):548-55.

Grandy J (1997) Efficient computation of volume of hexahedral cells. Lawrence Livermore National Laboratory, UCRL-ID-128886, doi:10.2172/632793.

James KA, Kennedy GJ, Martins JRRA (2014) Concurrent aerostructural topology optimization of a wing box. Computers and Structures 134(1):1–17.

James KA, Martins JRRA (2012) An isoparametric approach to level set topology optimization using a body-fitted finite element mesh. Computers and Structures 90-91(1):97-106.

Jang G-W, Kim YY, Choi KK (2004) Remesh-free shape optimization using the wavelet-Galerkin method. International Journal of Solids and Structures 41(22-23):6465–6483.

Krog L, Grihon S, Marasco A (2009) Smart design of structures through topology optimization. 8th World Congress on Structural and Multidisciplinary Optimization, Lisbon, Portugal, June 1-5.

Krog L, Tucker A, Kemp M, Boyd R (2004) Topology optimization of aircraft wing box ribs. 10th AIAA/ISSMO Multidisciplinary Analysis and Optimization Conference, Albany, New York.

Maute K, Allen M (2004) Conceptual design of aeroelastic structures by topology optimization. Structural and Multidisciplinary Optimization 27(1):27-42.

Min C, Gibou F (2007) Geometric integration over irregular domains with application to level-set methods. Journal of Computational Physics 226(2):1432-1443.

Niu M (1988) Airframe Structural Design, Conmilit Press Ltd., Hong Kong.

Oktay E, Akay HU, Merttopcuoglu O (2011) Parallelized structural topology optimization and CFD coupling for design of aircraft wing structures. Computers and Fluids 49(1):141-145.

Oktay E, Akay HU, Sehitoglu OT (2014) Three-dimensional structural topology optimization of aerial vehicles under aerodynamic loads. Computers and Fluids 92(1):225-232.

Osher S, Fedkiw R (2003) Level set methods and dynamic implicit surfaces. Springer, New York.

Rodden WP, Taylor PF, McIntosh Jr SC (1998) Further refinement of the subsonic doublet-lattice method Journal of Aircraft 35(5):720-727.

Sethian JA (1999) Level set methods and fast marching methods, 2nd ed., Cambridge University Press, New York.

Sethian JA, Vladimirsky A (2000) Fast methods for the Eikonal and related Hamilton-Jacobi equations on unstructured meshes. Proceedings of the National Academy of Sciences of the United States of America 97(11):5699-5703.

Stanford B, Beran P "Optimal structural topology of a platelike wing for subsonic aeroelastic stability," Journal of Aircraft, Vol. 48, No.4, 2011, pp. 1193-1203.

Stanford B, Dunning PD (2014) Optimal Topology of Aircraft Rib and Spar Structures under Aeroelastic Loads. Journal of Aircraft (Accepted). Doi: 10.2514/1.C032913.

Stanford B, Ifju P (2009) Aeroelastic topology optimization of membrane structures for micro air vehicles. Structural and Multidisciplinary Optimization 38(3):301-316.

Taminger K, Hafley R (2003) Electron Beam Freeform Fabrication: A Rapid Metal Deposition Process, Proceedings of the 3rd Annual Automotive Composites Conference, Troy, MI, September 9-10.

van Dijk NP, Maute K, Langelaar M, van Keulen F (2013) Level-set methods for structural topology optimization: a review. Structural and Multidisciplinary Optimization 48(3):437-472.

Vassberg J, DeHaan M, Rivers S, Wahls R (2008) Development of a common research model for applied CFD validation studies. AIAA Applied Aerodynamics Conference, Honolulu, Hawaii, August 10-13.

Wakayama S, Kroo I (1995) Subsonic wing planform design using multidisciplinary optimization. Journal of Aircraft, 32(4):746-753.

Wang MY, Wang X, Guo D (2003) A level set method for structural topology optimization. Computer Methods In Applied Mechanics and Engineering 192(1-2):227–246.

Wei P, Wang MY, Xing X (2010) A study on X-FEM in continuum structural optimization using a level set model. Computer-Aided Design 42(8):708-719.

Xing X, Wei P, Wang MY (2010) A finite element-based level set method for structural optimization. International Journal For Numerical Methods in Engineering 82(7):805-842.

Yamasaki S, Nishiwaki S, Yamada T, Izui K, Yoshimura M (2010) A structural optimization method based on the level set method using a new geometry-based re-initialization scheme. International Journal For Numerical Methods in Engineering 83(12):1580-1624.